ACS Catalysis

Research Article

pubs.acs.org/acscatalysis

Synthesis, Characterization, and Photocatalytic Activity of Y-Doped CeO_2 Nanorods

Anjalee D. Liyanage,[†] Sanjaya D. Perera,[†] Kui Tan,[‡] Yves Chabal,[‡] and Kenneth J. Balkus, Jr*[,†]

[†]Department of Chemistry and [‡]Laboratory for Surface and Nanostructure Modification, Department of Material Science and Engineering, The University of Texas at Dallas, 800 West Campbell Rd, Richardson, TX 75080-3021, United States

Ⓢ *Supporting Information*

ABSTRACT: Yttrium-doped ceria (YDC) nanorods were prepared by hydrothermal synthesis and characterized using Raman, UV−vis, transmission electron microscopy, scanning electron microscopy/energy-dispersive X-ray spectroscopy, X-ray photoelectron spectroscopy, and X-ray powder diffraction. The ceria nanorods showed an increase in the amount of oxygen vacancies with an increase in the Y concentration. When the doping level is <30%, the optical band gap of the doped ceria is lower than that of pure ceria nanorods. At < 50% of Y doping, the composite nanorods exhibited a higher photocatalytic activity for the degradation of model organic dyes compared to the pure ceria at room temperature, and the catalyst with 10% loading showed the maximum photocatalytic efficiency. However, at 100 °C, the photocatalytic activity significantly improved for all the nanorods with different Y loadings, and the greatest improvement was obtained for the sample with the highest number of oxygen vacancies.

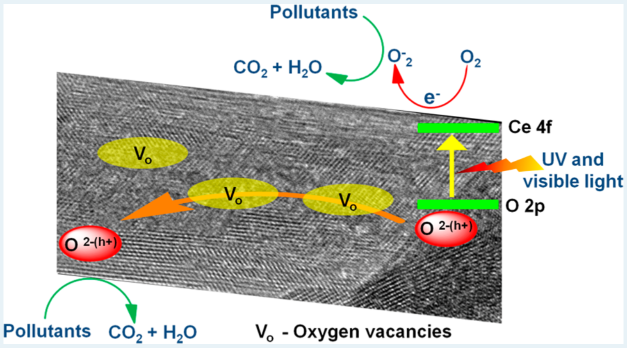

KEYWORDS: *Y-doped ceria, photocatalysis, oxygen vacancies, high-temperature photodegradation, photothermocatalysis*

■ INTRODUCTION

Semiconductor-based photocatalysts have shown promise for water/air purification.[1] These materials are widely used in treatment of wastewater, especially dyes, due to their low cost, low toxicity, recyclability, and the ability to facilitate multi-electron transfer processes. Many semiconductor photocatalysts have tunable properties that can be modified by size reduction, doping, and so forth.[2] Photocatalysis depends on the photogeneration of charge carriers and the efficient transfer of an electron or hole. The efficiency of the photocatalyst is mainly determined by the recombination rates of the photogenerated charge. The recombination rates are generally much faster (nanoseconds) than the interfacial transfer rate (microseconds to milliseconds) where many charge carriers recombine releasing energy as heat, thereby limiting the overall quantum efficiency of the photocatalyst.[3] By preventing or controlling the recombination of charge carriers, the photocatalytic activity of semiconductor metal oxides can be significantly improved. If a surface defect which can trap the electron or hole or any scavenger can be introduced to the system, the electron−hole recombination can be limited. The oxygen vacancies can act as electron capture centers.[4−6] Further, they can act as specific reaction sites for certain molecules in heterogeneous catalysis as they can bind adsorbates more strongly than normal oxide sites and also assist in their dissociation.[7,8] Therefore, the introduction of oxygen vacancies or increasing the density of oxygen vacancies at the surface of the photocatalyst can inhibit the recombination of electron−hole pairs while improving the photocatalysis. The oxygen vacancies can also bind oxygen, which acts as an electron scavenger and can generate superoxide radicals.

Cerium oxide (CeO_2) has been widely used for catalysis.[9−16] The catalytic properties and oxide ion conductivity of ceria originates from its fluorite type structure and the partial reduction of Ce^{4+} to Ce^{3+}, which gives rise to oxygen vacancies.[17] Further, CeO_2 has a band gap (3.2 eV) similar to TiO_2 (anatase) and holds promise as a suitable photocatalyst for the degradation of organic pollutants.[18−23] When ceria is doped with transition metals such as Fe, Mn, and Co, an improvement in photocatalytic activity was ascribed to an enhancement in the mobility of excitons, thus facilitating surface reactions.[24] This was evidenced by a red shift for the absorption bands of doped ceria, due to transition from O 2p to the lower energy unoccupied orbitals of the dopants. Recently Li, et al. studied the photocatalytic activity of mesoporous nanorod-like ceria at elevated temperatures (160−240 °C), and a higher photocatalytic efficiency due to the coupling of oxygen ion conduction with the photocatalysis was observed. The significantly enhanced mobility of oxygen ions at higher temperatures results in better separation of photogenerated electrons and holes, thereby improving the overall efficiency of the catalyst.[25]

Received: October 7, 2013
Revised: December 16, 2013
Published: January 3, 2014

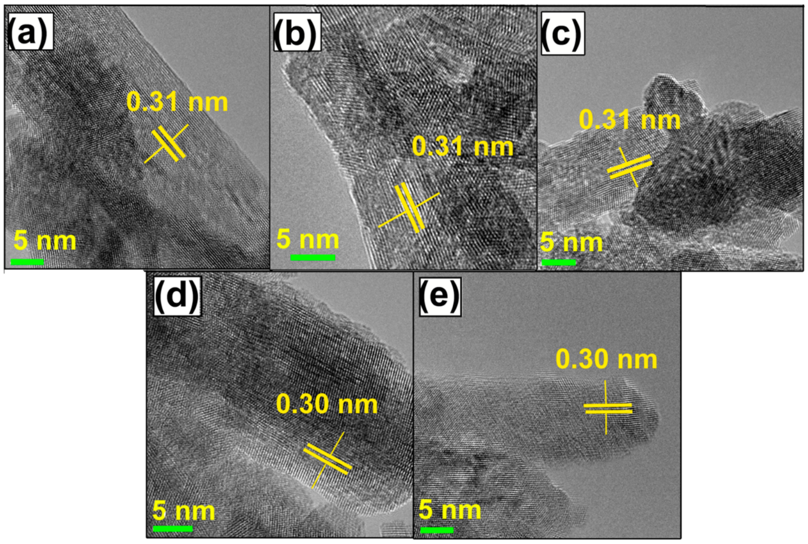

Figure 1. TEM images of pure ceria and YDC nanorods after calcination at 200 °C: (a) pure ceria, (b) $Ce_{0.89}Y_{0.11}O_{1.94}$, (c) $Ce_{0.73}Y_{0.27}O_{1.86}$, (d) $Ce_{0.56}Y_{0.44}O_{1.78}$, and (e) $Ce_{0.44}Y_{0.56}O_{1.72}$.

Most reported photocatalytic experiments are conducted at room temperature. However, solar heterogeneous photocatalytic detoxification generally operates at much higher temperatures. In solar photochemical processes, high-energy short-wavelength photons are collected to promote photochemical reactions. Most of these systems use UV or near-UV sunlight (300−400 nm) but this may go up to 580 nm (photo-Fenton heterogeneous photocatalysis).[26,27] The temperature inside these reactors can easily reach 40−50 °C, and during the summer, 70−80 °C is typical. Higher temperatures will favor mobility of oxygen vacancies with increased photocatalytic activity.

Doping trivalent rare-earth oxides in ceria creates oxygen vacancies.[28] The doping of ceria with Y has been well studied specially for solid oxide fuel cells.[29] In this paper, yttrium-doped ceria (YDC) nanorods were prepared and tested for the photocatalytic degradation indigo carmine and rhodamine B. The catalytic efficiency for the degradation of the dyes was evaluated at different Y dopant concentrations. At room temperature, the photocatalytic activity was higher compared to pure ceria up to 50% Y doping and then decreased with further Y loading. The photocatalytic efficiency of the catalysts was then studied at 100 °C. The photocatalytic efficiency improved with the number of oxygen vacancies. The catalyst with the highest number of oxygen vacancies showed a 20-fold higher activity compared to the room temperature photocatalytic activity for the same catalyst loading.

■ EXPERIMENTAL DETAILS

Synthesis of YDC nanorods. The 1D YDC nanorods were synthesized using a modified hydrothermal method.[30] In a typical procedure, a solution having the molar ratio of Ce/Y = 9:1 was prepared by dissolving 2.60 g of $Ce(NO_3)_3{\cdot}6H_2O$ (5 mmol) and 0.203 g of $Y(NO_3)_3.6H_2O$ (0.56 mmol) in 5 mL of DI water. Then, a solution of 14 M NaOH (7.35 g in 10 mL) was added. The pH of the final solution was 14. The slurry formed was transferred to a Teflon reactor (17.5 mL) and autoclaved at 110 °C for 24 h. The resulting product was isolated by centrifugation and washed three times with deionized water and dried at 80 °C for 24 h. The product was calcined in air at 200 °C for 1 h. The preparations of other YDC nanorods were carried out using the same procedure with different molar ratios of the metal precursors. The solid solutions are denoted as $Ce_{1-x}Y_xO_{2-x/2}$ $(0 < x < 1)$ where the dopant concentrations are $x = 0, 0.1, 0.3, 0.5, 0.7$.[28]

Characterization. X-ray powder diffraction (XRD) patterns were recorded on a Rigaku Ultima IV diffractometer employing Cu Kα radiation. Transmission electron microscope (TEM) images were obtained using a FEI CM200 FEG transmission electron microscope operating at 200 kV. Raman spectra were recorded in the region of 200−800 cm^{-1} using a Jobin Yvon Horiba high-resolution LabRam Raman microscope system equipped with a Spectra-Physics model 127 helium−neon laser operating at 35 mW for the 633 nm output as the excitation source. The optical absorption spectra of the catalysts with different doping levels were measured from 400 to 800 nm using a Perkin-Elmer Lambda 900 UV−vis/NIR spectrophotometer. Scanning electron microscope (SEM) images and energy-dispersive spectra (EDS) were collected using a Zeiss Supra TM variable-pressure-field emission scanning electron microscope. Zeta potential of YDC nanorods was measured using Zetasizer Nano ZS using dispersions of nanorods in water. X-ray photoelectron spectroscopy (XPS) measurements were carried out in a Perkin-Elmer PHI System. The photoelectrons are excited by using an Al Kα (1486.6 eV) X-ray source at a chamber base pressure of 1.5×10^{-9} Torr, and the spectra were recorded using a 16-channel detector with a hemispherical analyzer.

Photodegradation of Organic Dyes. The photocatalytic activity was evaluated for the photodegradation of the organic dyes indigo carmine and rhodamine B. The reaction was carried out in a dark box containing a water-cooled 450 W Hanovia low-pressure quartz mercury lamp. A 250 mL quartz round-bottom flask was placed 15 cm from the light source containing a mixture of 20.5 mg of catalyst and 100 mL of a 15.5 mg/L dye solution. The photodegradation of indigo carmine was tested at room temperature and atmospheric pressure. First, the reaction mixture was stirred in the dark for 30 min to ensure complete equilibration of the adsorption/desorption of the organic dye by the catalyst. The mixture was then irradiated for 20 min, and 5 mL aliquots were collected, followed by centrifugation to remove the catalyst particles. The supernatant was used to determine the concentration of residual dye by UV−vis spectroscopy based on the absorbance at 610 nm. This procedure was triplicated for each sample. The photodecomposition of rhodamine B was carried out in the same manner except that the concentration of the dye solution was 5.0 mg/L, the amount of catalyst used was 20 mg, and the equilibration was carried out for 1 h.

To study the photodecomposition of the dye at higher temperature, 20.5 mg of the catalyst was stirred in a 250 mL quartz round-bottom flask containing 100 mL 32 mg/L indigo carmine solution. A reflux condenser was attached to the round-bottom flask, and the solution was refluxed for 1 h in the dark to ensure the complete equilibration of the dye with the catalyst. Then the mixture was irradiated at reflux, and 5 mL aliquots were collected every 10 min, followed by centrifugation to remove the catalyst particles prior to UV−vis analysis. Control experiments were carried out under the same conditions but without light.

■ RESULTS AND DISCUSSION

Characterization of Ceria and Y-Doped Ceria Nanorods. The morphologies of as-prepared CeO_2 nanorods were determined using transmission electron microscopy (Supporting Information, Figure S1). Figure 1a shows a close-up TEM image of the ceria nanorods after annealing at 200 °C. The annealed ceria nanorods were an average 100 ± 37 nm in length and 10.9 ± 2.8 nm in diameter. Figure 1b−e show the TEM images of the Y-doped nanorods having the compositions of $Ce_{0.89}Y_{0.11}O_{1.94}$, $Ce_{0.73}Y_{0.27}O_{1.86}$, $Ce_{0.56}Y_{0.44}O_{1.78}$, and $Ce_{0.44}Y_{0.56}O_{1.72}$, respectively. The addition of Y to ceria at a loading of ~10% (Figure 1b) results in a decrease in size to 40.0 ± 5.2 and 8.4 ± 1.1 relative to pure ceria. At higher loadings of yttrium, the size of the nanorods increased but still not as large as CeO_2. For $Ce_{0.73}Y_{0.27}O_{1.86}$, $Ce_{0.56}Y_{0.44}O_{1.78}$, and $Ce_{0.44}Y_{0.56}O_{1.72}$, the measured lengths were 40.0 ± 6.5, 52.3 ± 9.7, and 70.0 ± 25.3 nm, respectively (Supporting Information, Figure S1). The widths for $Ce_{0.73}Y_{0.27}O_{1.86}$, $Ce_{0.56}Y_{0.44}O_{1.78}$, and $Ce_{0.44}Y_{0.56}O_{1.72}$ were 8.4 ± 1.3, 11.5 ± 2.6, and 13.1 ± 2.7 nm, respectively. A similar trend was observed by Yang et al. for the growth of Y-doped nanorods with an increase in Y loading.[28] The lattice fringes of the nanorods are clearly visible with a *d*-spacing of 0.3139, 0.3144, 0.3130, 0.3114, and 0.3110 nm for ceria $Ce_{0.89}Y_{0.11}O_{1.94}$, $Ce_{0.73}Y_{0.27}O_{1.86}$, $Ce_{0.56}Y_{0.44}O_{1.78}$, and $Ce_{0.44}Y_{0.56}O_{1.72}$, respectively. This is attributed to the (111) planes of ceria (JCPDS 34-0394).

The compositions of the annealed nanorods were determined by Energy Dispersive X-ray spectra (Supporting Information, Figure S2−S5). The results are generally consistent with the expected ratio between Ce and Y based on the synthesis gel. However, for the sample $Ce_{1-x}Y_xO_{2-x/2}$ where x is 0.7, the actual amount was found to be 0.56. The synthesis reactions were carried out at pH 14 and at a relatively high supersaturation. Some yttrium hydroxide ($Y(OH)_3$) may have precipitated and was partially removed during the washing step with slightly acidic deionized water resulting in a lower amount of Y in the final product.[31]

Figure 2 shows XRD patterns of as-synthesized nanorods. The pure ceria nanorods can be indexed to cubic structure (JCPDS 34-0394), which has characteristic peaks at 28.42°, 32.97°, 47.42°, and 56.23° 2θ.[15,28] During the nanorod formation, first $Ce(OH)_3$ nanorods are formed, and then the outer surface is oxidized forming CeO_2.[30] When Y is introduced to the synthesis, the formation of both $Ce(OH)_3$ and $Y(OH)_3$ can be observed for the as-synthesized nanorods, as shown in Figure 2. With the introduction of higher amounts of Y, the characteristic peaks become sharper and shift toward higher 2θ values, indicating the formation of the solid solutions of $Ce_{1-x}Y_x(OH)_3$ $(0 < x < 1)$.[28]

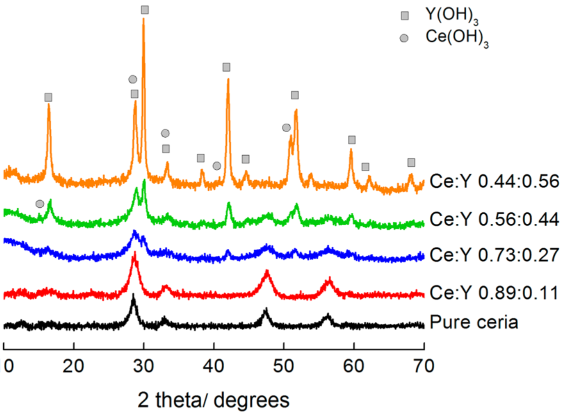

Figure 2. XRD pattern of as-prepared nanorods.

Figure 3 shows the XRD patterns for the samples after calcination at 200 °C for 1 h. The only diffraction peaks observed are for ceria. This further confirms the formation of a single phase resulting in successful doping of Y into ceria. When Y^{3+} is doped into the ceria lattice structure, the lattice parameter decreases with increasing Y concentration, as previously observed.[32] Further, the lattice parameters are comparable to calculated values.[29,33] This trend may reflect an increase in oxygen vacancy concentration with increasing Y content, even though the ionic radius of Y^{3+} is slightly larger than that of Ce^{4+} (1.019 and 0.97 Å, respectively). Additionally the effective anionic radius in the fluorite lattice decreases with an increase in the number of oxygen-ion vacancies.[34] This further confirms that the Y ions are incorporated into the ceria lattice forming fluorite-like solid solutions. The Figure 3 inset shows the (111) reflection shifts toward higher 2θ values with increasing concentrations of yttrium. The calculated *d*-spacing

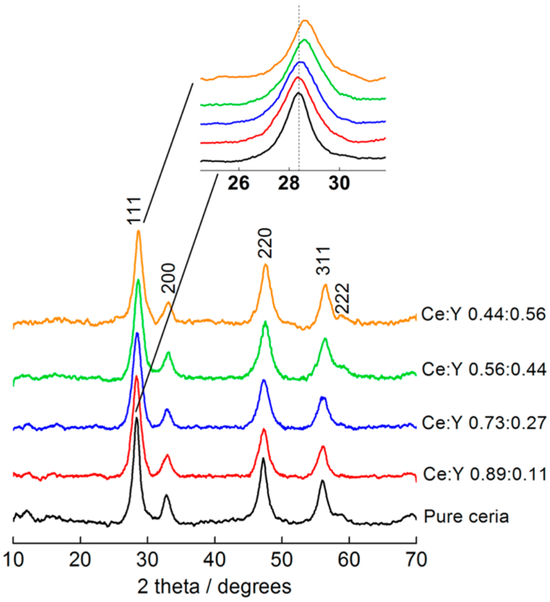

Figure 3. XRD patterns of the nanorods after annealing at 200 °C.

values are comparable with the values obtained using TEM. The calculated lattice parameter *a* values for $Ce_{0.89}Y_{0.11}O_{1.94}$, $Ce_{0.73}Y_{0.27}O_{1.86}$, $Ce_{0.56}Y_{0.44}O_{1.78}$, and $Ce_{0.44}Y_{0.56}O_{1.78}$ were 5.446, 5.421, 5.394, and 5.387 Å, respectively.

The presence of Ce^{3+} or Y^{3+} in the fluorite structure of CeO_2 generates oxygen vacancies in order to maintain electroneutrality.[21] The oxygen vacancies were characterized using Raman spectroscopy (Figure 4). Usually bulk ceria has a strong Raman band at 465 cm^{-1}, which is attributed to Raman active vibrational mode (F_{2g}) of fluorite-type structure. The Raman spectra of all samples show a strong band around this region, confirming the existence of fluorite structure in all the doped samples.

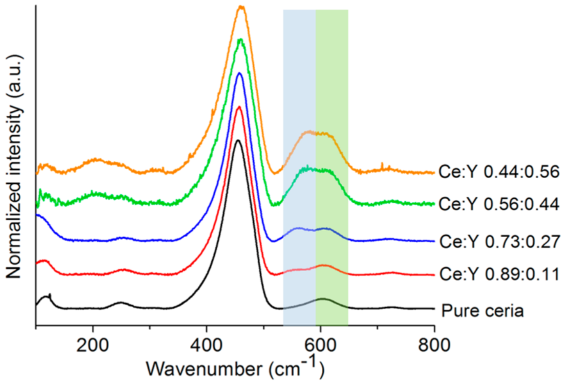

Figure 4. Raman spectra of the nanorods with different ratios of Ce/Y.

The band at ~600 cm^{-1} (green stripe) is related to the oxygen vacancies due to the presence of Ce^{3+} in the CeO_2 lattice and defects caused by small size effects.[36] The intensity of this band also increases with increasing Y concentration and may be due to the formation of Ce^{3+} ions in order to accommodate Y^{3+} ions in the ceria host.[35] However, with the introduction of Y^{3+} into the lattice, another peak appears around ~565 cm^{-1} (blue stripe), and the band intensity increases as the amount of yttria increases. This band is attributed to extrinsic oxygen vacancies that are generated due to the substitution of tetravalent Ce^{4+} with trivalent Y^{3+}.[36] When there is ~10% of Y, there is only a small band for extrinsic oxygen vacancies. However, as the Y concentration becomes higher, the peak at 565 cm^{-1} increases, indicating the generation of extrinsic oxygen vacancies. Table 1 lists the intensity ratio between the 565 and 460 cm^{-1} bands (I_{565}/I_{465}), revealing a continuous increase in oxygen vacancies in the doping range $0.0 \leq x \leq 1.0$. The O1s XPS spectra were also collected (Figure S9), but the interpretation was complicated by adsorbed oxygen species.

Table 1. Band Gap Energy and the Relative Intensity of the Typical Peak for Extrinsic Oxygen Vacancies of Raman Spectra

sample	band gap (eV)	I_{565}/I_{460}
ceria	2.68	
$Ce_{0.89}Y_{0.11}O_{1.94}$	2.62	0.039
$Ce_{0.73}Y_{0.27}O_{1.86}$	2.66	0.088
$Ce_{0.56}Y_{0.44}O_{1.78}$	2.75	0.130
$Ce_{0.44}Y_{0.56}O_{1.72}$	2.82	0.260

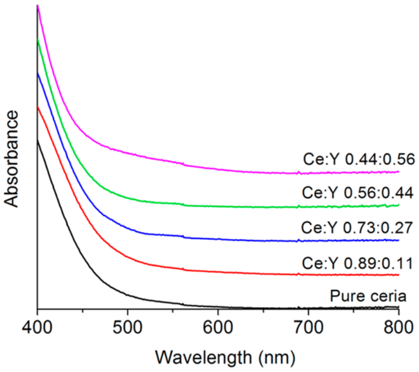

Figure 5. UV−vis diffuse reflectance spectra of the composites with different ratios of Ce:Y.

The UV−vis diffuse reflectance spectra (DRS) shown in Figure 5 were used to calculate the band gaps of the Y-doped and pure CeO_2 nanorods. The optical band gap energies of the nanorods were calculated using the formula Eg = 1240/λ (nm), where λ is the wavelength corresponding to the absorption onset. The optical band gap energies of the nanorods are shown in Table 1. Upon doping, the band gap initially decreases then becomes larger than CeO_2 at 2.68 eV. The colors of all the samples after annealing were yellowish. The $Ce_{0.89}Y_{0.11}O_{1.94}$ sample had the highest intensity yellow color, and the nanorods became more white with increasing amounts of Y. In all cases, the nanorods exhibit a lower band gap energy compared to bulk CeO_2 (3.2 eV). This could be explained by the formation of localized states within the band gap due to oxygen vacancies and increased Ce^{3+} ion concentration.[35,37] Previously, it has been shown that the presence of Ce^{3+} reduces the band gap leading to a red shift.[25] The absorption of Y-doped ceria red shifts at lower dopant concentrations. It has been reported that this shift indicates substitution of Y ions with Ce^{4+} ions forming Ce^{3+}, which increases the oxygen vacancy concentration of Ce-based materials due to a charge compensation mechanism.[38] However, when the dopant concentration is ≥50%, the band gap energy increases resulting in a blue shift in the absorption compared to pure ceria. A similar behavior was observed for other rare-earth ion-doped ceria solid solutions as well. Xiao et al. observed that doping ceria with cations such as Y^{3+} partially suppresses the conversion of Ce^{4+} to Ce^{3+}.[39] According to the Ce XPS data (Figure S8), a similar trend was observed. The XPS Ce $3d_{5/2}$ and $3d_{3/2}$ doublets are usually denoted as u and v. The Ce 3d spectra can be deconvoluted into four pairs of the spin−orbital doublet peaks ($3d_{5/2}$ and $3d_{3/2}$): v/u; v′/u′; v″/u″; v‴/u‴, where v/u, v″/u″, and v‴/u‴ peaks refer to the characteristic Ce^{4+} 3d final states, and v′/u′ corresponds to Ce^{3+} 3d final states.[40,41] The presence of Ce^{3+} is due to the reduction of Ce^{4+} in the oxide structure.[42] The faction of Ce^{3+} species can be estimated using relative areas of v′/u′ peaks according to the equation:[41,42]

$$[\mathrm{Ce}^{3+}] = \frac{S_{v'} + S_{u'}}{\sum (S_v + S_u)}$$

where *S* is the integrated area corresponding to peak v^i or u^I. The calculated ratio of Ce^{3+} for the CeO_2, $Ce_{0.89}Y_{0.11}O_{1.94}$, $Ce_{0.73}Y_{0.27}O_{1.86}$, $Ce_{0.56}Y_{0.44}O_{1.78}$, and $Ce_{0.44}Y_{0.56}O_{1.78}$ are 13.47, 11.40, 10.70, 7.27, and 5.82%, respectively. Therefore, the relative content for Ce^{3+} in the oxides decreased after increasing the doping level of Y^{3+}, which is consistent with a previous report and attributed to the substitution of Y^{3+} for Ce^{3+}.[28]

When the amount of dopant concentration is high, the partial reduction of Ce^{4+} to Ce^{3+} becomes comparatively lower and the amount of intrinsic oxygen vacancies becomes lower compared to the amount of extrinsic oxygen vacancies, which is also evident from the Raman spectra for YDCs. This may be the reason for higher band gaps observed for high dopant concentrations.[15,39]

Photocatalytic Performance of Y-Doped Ceria Samples. The isoelectric point of Y_2O_3 particles is ∼9.4, and hydrous cerium oxide is 6.75−8.[43,44] According to the experimental data, the isoelectric point of pure ceria nanorods was 4.70, and the isoelectric point of the doped material was found to be 6.4−6.5. There was not a huge variation with the amount of Y^{3+} (data not shown). In this study, the pH of the dye solution maintained at 6, which is closer to the pH of the dye wastewater as reported in a few studies.[45,46] The surface state of the ceria could depend on the pH of the medium. If the pH of the solution is greater than the isoelectric point of ceria, the surface becomes negatively charged, and when it is lower than the pH of the solution, the surface becomes positively charged. Since the isoelectric point of the doped material is higher than the pH of the dye solution, the surface is assumed to be positively charged. Hence, the anionic dyes have a greater affinity toward the catalyst. In this study, the photodegradation of both anionic (indigo carmine) and cationic (rhodamine B) dyes was tested.

Figure 6 shows the photocatalytic degradation of the anionic dye indigo carmine in a quartz reactor over 100 min with samples of different dopant concentrations. $Ce_{0.89}Y_{0.11}O_{1.94}$, $Ce_{0.73}Y_{0.27}O_{1.86}$, and $Ce_{0.56}Y_{0.44}O_{1.78}$ exhibit higher photocatalytic activity compared to pure ceria. According to Figure 6, the $Ce_{0.89}Y_{0.11}O_{1.94}$ sample has the highest photocatlytic activity and shows 20% higher degradation compared to pure ceria nanorods. However, the photocatalytic efficiency decreases with higher amounts of oxygen vacancies at room temperature. That means when the nanorods are doped <50%, they show a higher photocatalytic activity compared to pure ceria nanorods. But when the amount of Y is further increased, the activity goes down dramatically. The separation of electron−hole pairs is related to the amount of oxygen vacancies present in the catalyst. The number of oxygen vacancies increases with increasing amounts of Y. According to Mori et al., when more oxygen vacancies are generated, the probability of the cations sitting in close proximity to each other was increased. Therefore, all the existing mobile oxygen vacancies come together to form deep traps, and small microdomains may be generated due to the ordering of isolated cations and oxygen vacancies in the lattice.[47,48] Generation of these deep traps again would allow fast electron−hole recombination, thereby decreasing the photocatalytic efficiency. A similar effect was observed for TiO_2, where it was found that surface defects (oxygen vacancies) act as charge carrier traps and adsorption sites where the charge transfer to adsorbed species can prevent the electron−hole recombination. On the other hand, bulk defects act as charge carrier traps where the electron−hole recombines.[49] Therefore, at room temperature, the oxygen vacancies at low doping levels promote the photocatalytic activity of ceria, but with increasing doping levels, it becomes worse. It was found that at room temperature, only below 50% Y doping is favorable for the efficient photocatalysis, where ∼10% was found to be the optimum doping level with the optimum number of oxygen vacancies that gives the highest photocatalytic activity (Figure S7).

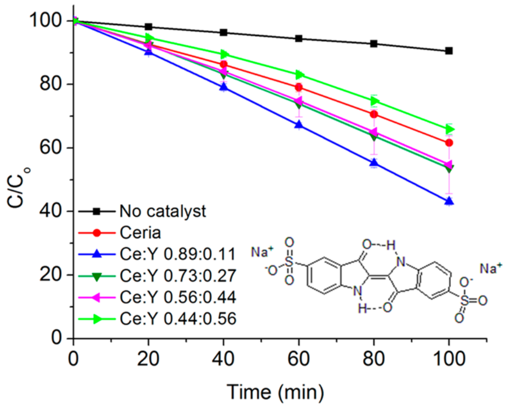

Figure 6. Photocatlytic degradation of indigo carmine dye with different Y-doped ceria samples.

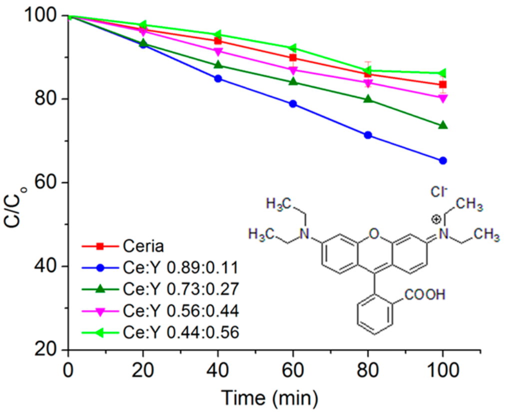

Figure 7. Photocatalytic degradation of rhodamine B dye with different Y-doped ceria nanorods.

The cationic dyes rhodamine B was also tested as a model substrate, as shown in Figure 7. In this study, also the catalyst $Ce_{0.89}Y_{0.11}O_{1.94}$ showed the highest photocatalytic activity with rhodamine B. Interestingly, it followed a similar pattern for the degradation of dye compared to indigo carmine (Figure 7). However, the catalytic efficiency for all the catalysts was lower compared to degradation of anionic dyes. In this study, because the pH of the dye solution maintained at pH 6 and the surface of the catalyst is positively charged, the anionic dyes have a greater affinity toward the catalyst. This may be the reason for the higher photodegradation efficiency of the YDC nanorods toward anionic dyes. According to these results, it can be concluded that Y-doped ceria nanorods are a good catalyst toward the photodecomposition of both anionic and cationic dyes, but anionic dyes have a greater affinity toward the catalyst, resulting in a much higher photodegradation.

At high temperatures, the oxygen vacancies may become mobile and not form deep trap sites. Therefore, the degradation of indigo carmine was carried out at 100 °C (Figure 8). At 100 °C, all catalysts degraded the dye faster than at room temperature. The stability of the catalysts after refluxing in water for several hours was studied using TEM (data not

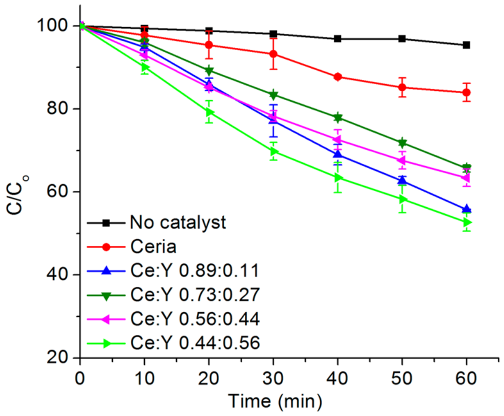

Figure 8. Photocatalytic degradation of indigo carmine at 100 °C.

shown), and the nanorods remained intact. As expected, doped ceria nanorods had a much higher photocatalytic activity at elevated temperature compared to pure ceria nanorods. This is because of the presence of higher amounts of oxygen vacancies and the enhanced oxygen ion mobility at 100 °C. The sample with the highest amount of Y exhibited the highest photocatalytic activity. When the amount of Y decreased, the activity was diminished as well. However, nanorods with ~10% doping showed activity similar to the nanorods with 56% doping.

In order to prove that the enhanced degradation of dye at high temperature was due to photocatalysis, experiments were carried out in the absence of light, and only very low catalytic activities were observed (Figure S6). The catalytic activity slightly improved with doping up to 44% and then decreased.

Previously, Li et al. demonstrated that at high temperatures (160−240 °C), the separation of charge carriers in mesoporous ceria is higher, resulting in higher photocatalytic efficiency.[25] Usually the charge separation efficiency in semiconductor materials is mainly governed by lattice (phonon) scattering. Phonons can be simply defined as the pressure waves that are generated within the crystal at any temperature due to vibrating lattice ions or atoms. When these phonons collide with electrons or holes, they scatter. When the temperature increases, the ions/atoms start to vibrate strongly, giving rise to more phonons. Therefore, the scattering of electrons/holes increases within the lattice leading to recombination of photogenerated carriers.[25] When ceria is irradiated, electrons are excited from the O_{2p} valence band to an empty conduction (Ce_{4f}), forming the $Ce^{4+(e-)}$ and $O^{2-(h+)}$ pair.[21,50] The photogenerated holes get trapped on oxygen ions, whereas electrons are localized on cerium ions. The photogenerated electrons reduce adsorbed electron acceptors (e.g., O_2) forming superoxide radicals, and the holes oxidize organic substances adsorbed on the catalyst or react with water forming hydroxyl radicals, which can also be involved in the decomposition of the organic substrates.[26] When the number of oxygen vacancies is higher, the oxygen ion mobility gets higher. Further, it was shown that the increase in temperature can also increase the mobility of the oxygen ions.[51] The transportation mobility of the lattice oxygen ions rather than lattice vibrations is beneficial for the separation of photogenerated electrons and holes, which ultimately leads to higher photocatalytic activity.

The photocatalytic degradation reaction is assumed to follow a pseudo-first order reaction where $-\ln(C/C_0) = k_t$, and k is the apparent reaction rate constant (min^{-1}) (Figure 9). The rate constant for the photocatalytic activity at room temperature is denoted as k_p, while the rate constants for thermocatalytic reactions and photothermocatalytic reactions are denoted as k_t and k_{pt}, respectively. The highest rate constant for photothermocatalytic activity (0.0104 min^{-1}) was obtained for the sample $Ce_{0.44}Y_{0.56}O_{1.72}$, which has the highest amount of extrinsic oxygen vacancies (Table 2). The rate improvement was ~22 times compared to the same catalyst at room temperature. The rate constant k_t is 0.0035 min^{-1}, which is ~one-third of the photothermocatalytic decomposition at the same temperature. If the photothermocatalytic reaction is assumed to be due to the photocatalytic degradation in parallel with the thermocatalytic degradation that proceeds independently, then, $\mathrm{d}C/\mathrm{d}t = k_pC + k_tC$, where k_{pt} should be equal to $k_p + k_t$. However, this value (0.004 min^{-1}) was 2.6 times lower than k_{pt}. This further confirms the efficient electron hole separation at high temperatures due to the mobility of oxygen ions leading to a synergistic effect for the degradation of the dye. For all samples, the sum of k_t+ k_p was lower compared to k_{pt}. Even though $Ce_{0.89}Y_{0.11}O_{1.94}$ has the highest activity at room temperature, the k_{pt} was improved by only ~5.0 times at 100 °C. The increase in the rate constant compared to room temperature for $Ce_{0.73}Y_{0.27}O_{1.86}$ and $Ce_{0.56}Y_{0.44}O_{1.78}$ was ~5 and ~6 times, respectively. Thus, there is clear improvement in photocatalysis at high temperatures with an increase in oxygen vacancies.

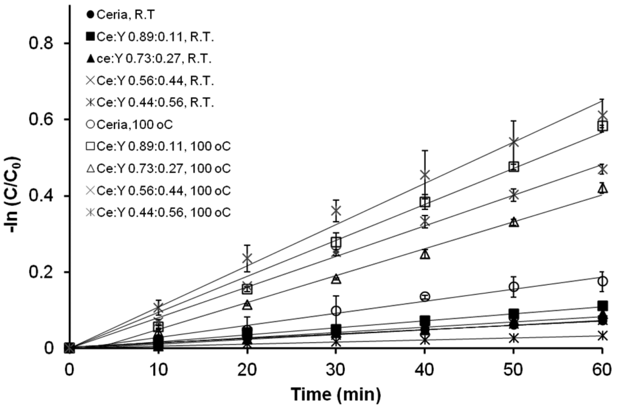

Figure 9. Plot of $-\ln(C/C_0)$ vs irradiation time at 100 °C and at room temperature.

It has been reported that above 80 °C, the exothermic adsorption of reactants becomes disfavored, and hence the photocatalytic efficiency becomes low for TiO_2.[27] However, according to the results obtained, for YDC nanorods the separation efficiency of electrons and holes at high temperature outweighs any loss in adsorption of the reactants on the catalyst, thereby improving the overall photocatalytic efficiency.

■ CONCLUSION

Y-doped ceria nanorods with different amounts of dopant were hydrothermally synthesized. An increase of the dopant concentration resulted in an increase in the amount of oxygen vacancies. The doped nanorods showed higher photocatalytic activity compared to ceria at lower levels of doping due to both low band gap energy and the presence of oxygen vacancies. However, when doped with more than 50% of Y, the nanorods showed a lower photocatalytic activity compared to pure ceria at room temperature, which may be due to fast electron−hole recombination, owing to the formation of microdomains of oxygen vacancy clusters. However, at higher temperature, the

Table 2. Rate Constant Values for Photocatalytic Degradation of Indigo Carmine at Room Temperature, Thermocatalytic Degradation at 100 °C, and Photothermocatalytic Degradation at 100 °C of Pure Ceria Nanorods and Y-Doped Ceria Nanorods

sample	rate constant $(k_p)/\text{min}^{-1}$	rate constant $(k_t)/\text{min}^{-1}$	rate constant $(k_{pt})/\text{min}^{-1}$
ceria	0.0011	0.0020	0.0032
Ce/Y 0.89:0.11	0.0018	0.0043	0.0094
Ce/Y 0.73:0.27	0.0014	0.0044	0.0071
Ce/Y 0.56:0.44	0.0013	0.0048	0.0080
Ce/Y 0.44:0.56	0.0005	0.0035	0.0104

photocatalytic efficiency was greatly improved, and the greatest improvement was obtained for the sample with the highest amount of oxygen vacancies. The significant enhancement in oxygen ion conductivity at high temperature can greatly enhance the charge separation, thereby improving the photocatalytic efficiency of dye degradation. Most catalytic experiments are conducted at room temperature, but solar reactors operate at higher temperatures such that there are opportunities to develop better catalysts that operate under these conditions.

■ ASSOCIATED CONTENT

Ⓢ Supporting Information

Supplemental TEM images, EDX spectra, thermocatalytic/photocatalytic degradation data, and XPS spectra, as referenced in the text. This material is available free of charge via the Internet at http://pubs.acs.org.

■ AUTHOR INFORMATION

Corresponding Author

*E-mail: Balkus@utdallas.edu.

Notes

The authors declare no competing financial interest.

■ ACKNOWLEDGMENTS

We would like to acknowledge the National Science Foundation (CBET-0854059) for financial support.

■ REFERENCES

(1) Chan, S. H. S.; Wu, T. Y.; Juan, J. C.; The, C. Y. *J. Chem. Technol. Biotechnol.* **2011**, *86*, 1130−1158.

(2) Chatterjee, D.; Dasgupta, S. *J. Photochem. Photobiol., C* **2004**, *112*, 269−278.

(3) Hoffmann, M. R.; Martin, S. T.; Choi, W. Y.; Bahnemann, D. W. *Chem. Rev.* **1995**, *95*, 69−96.

(4) Zhang, Z.; Wang, W.; Gao, E.; Shang, M.; Xu, J. *J. Hazard. Mater.* **2011**, *196*, 255−262.

(5) Wang, J. C.; Liu, P.; Fu, X. Z.; Li, Z. H.; Han, W.; Wang, X. X. *Langmuir* **2009**, *25*, 1218−1223.

(6) Tachikawa, T.; Yamashita, S.; Majima, T. *J. Am. Chem. Soc.* **2011**, *133*, 7197−7204.

(7) Pu, Z. Y.; Liu, X. S.; Jia, A. P.; Xie, Y. L.; Lu, J. Q.; Luo, M. F. *J. Phys. Chem. C* **2008**, *112*, 15045−15051.

(8) Gong, X. Q.; Selloni, A.; Batzill, M.; Diebold, U. *Nat. Mater.* **2006**, *5*, 665−670.

(9) Noronha, F. B.; Fendley, E. C.; Soares, R. R.; Alvarez, W. E; Resasco, D. E. *Chem. Eng. J.* **2001**, *82*, 21−31.

(10) Liu, X.; Zhou, K.; Wang, L.; Wang, B.; Li, Y. *J. Am. Chem. Soc.* **2009**, *131*, 3140−3141.

(11) Hayashi, F.; Iwamoto, M. *ACS Catal.* **2013**, *3*, 14−17.

(12) Trovarelli, A. *Catal. Rev. Sci. Eng.* **1996**, *38*, 439−520.

(13) Kaspar, J.; Fornasiero, P.; Graziani, M. *Catal. Today* **1999**, *2*, 285−298.

(14) Fu, Q.; Weber, A.; Flytzani-Stephanopoulo, M. *Catal. Lett.* **2001**, *77*, 87−95.

(15) Soykal, I. I.; Sohn, H.; Ozkan, U. S. *ACS Catal.* **2012**, *2*, 2335−2348.

(16) Meher, S. K.; Rao, G. R. *ACS Catal.* **2012**, *2*, 2795−2809.

(17) Tsunekawa, S.; Ishikawa, K.; Li, Z. Q.; Kawazoe, Y.; Kasuya, A. *Phys. Rev. Lett.* **2000**, *85*, 3440−3443.

(18) Arul, N. S.; Mangalaraj, D.; Chen, P. C.; Ponpandian, N.; Viswanathan, C. *Mater. Lett.* **2011**, *65*, 3320−3322.

(19) Xu, M.; Xie, S.; Lu, X.-H.; Liu, Z.-Q.; Huang, Y.; Zhao, Y.; Ye, J.; Tonga, Y.-X. *J. Electrochem. Soc.* **2011**, *158*, E41−E44.

(20) Tang, Z.-R.; Zhang, Y.; Xu, Y. J. *RSC Adv.* **2011**, *1*, 1772−1777.

(21) Hernandez-Alonso, M. D.; Hungrıa, A. B.; Martınez-Arias, A.; Fernandez-Garcıa, M.; Coronado, J. M.; Conesa, J. C.; Soria, J. *Appl. Catal., B* **2004**, *50*, 167−175.

(22) Zhai, Y.; Zhang, S.; Pang, H. *Mater. Lett.* **2007**, *61*, 1863−1866.

(23) Chen, F.; Cao, Y.; Jia, D. *Appl. Surf. Sci.* **2011**, *257*, 9226−9231.

(24) Yue, L.; Zhang, X.-M. *J. Alloys Compd.* **2009**, *475*, 702−705.

(25) Li, Y.; Sun, Q.; Kong, M.; Shi, W.; Huang, J.; Tang, J.; Zhao, X. *J. Phys. Chem. C* **2011**, *115*, 14050−14057.

(26) Malato, S.; Balnco, J.; Vidal, A.; Richter, C. *App. Catal. B* **2002**, *37*, 1−15.

(27) Malato, S.; Fernandez-Ibanez, P.; Maldonado, M. I.; Balnco, J.; Gernjak, W. *Catal. Today* **2009**, *147*, 1−59.

(28) Yang, D.; Wang, L.; Sun, Y.; Zhou, K. *J. Phys. Chem. C* **2010**, *114*, 8926−8932.

(29) Zhang, T. S.; Ma, J.; Huang, H. T.; Hing, P.; Xia, Z. T.; Chan, S. H.; Kilner, J. A. *Solid State Sci.* **2003**, *5*, 1505−1511.

(30) Pan, C.; Zhang, D.; Shi, L.; Fang, J. *Eur. J. Inorg. Chem.* **2008**, 2429−2436.

(31) Palard, M.; Balencie, J.; Maguer, A.; Hochepied, J.-F. *Mater. Chem. Phys.* **2010**, *120*, 79−88.

(32) Rey, J. F. Q.; Muccillo, E. N. S. *J. Eur. Ceram. Soc.* **2004**, *24*, 1287−1290.

(33) Huang, C. W.; Wei, W. C. J.; Chen, C. S.; Chen, J. C. *J. Eur. Ceram. Soc.* **2011**, *31*, 3159−3169.

(34) Bošković, S. B.; Djurović, D. R.; Zec, S. P.; Matović, B. Z.; Zinkevich, M.; Aldinger, F. *Ceram. Int.* **2008**, *34*, 2001−2006.

(35) Sarkar, M.; Rajkumar, R.; Tripathy, S.; Balakumar, S. *Mater. Res. Bull.* **2012**, *47*, 4340−4346.

(36) Goto, Y.; Takahashi, K.; Omata, T.; Otsuka-Yao-Matsuo, T. *J. Phys.: Conf. Ser.* **2009**, *165*, 1−4.

(37) Lu, X.; Li, X.; Chen, F.; Ni, C.; Chen, Z. *J. Alloys Compd.* **2009**, *476*, 958−962.

(38) Wang, J.; Tafen, D. N.; Lewis, J. P.; Hong, Z. L.; Manivannan, A.; Zhi, M. J.; Li, M.; Wu, N. Q. *J. Am. Chem. Soc.* **2009**, *131*, 12290−12297.

(39) Xiao, G. L.; Li, S.; Li, H.; Chen, L. Q. *Microporous Mesoporous Mater.* **2009**, *120*, 426−431.

(40) Francisco, M. S. P; Mastelaro, V. R.; Nascente, P. A. P.; Florentino, A. O. *J. Phys. Chem. B* **2001**, *105*, 10515−10522.

(41) Lubna, R. S.; Bakhtyar, A.; Hao, Z.; Wang, W. G.; Song, Y. Q.; Zhang, H. W.; Song, Y. Q.; Zhang, H. W.; Shah, S. I.; Xiao, J. Q. *J. Phys.: Condens. Matter* **2009**, *21*, 486004(1−9).

(42) Hierso, J.; Sel, O.; Ringuede, A.; Laberty-Robert, C.; Bianchi, L.; Grosso, D.; Sanchez, C. *Chem. Mater.* **2009**, *21*, 2184−2192.

(43) Kim, K.-Y.; Yun, Y.-H. *J. Ceram. Process. Res.* **2007**, *8*, 421−426.

(44) Liu, K.-S.; Chowdhary, S. *Int. J. Mol. Sci.* **2010**, *11*, 3226−3251.

(45) Shin, S. H.; Kim, Y. H.; Jung, S. K.; Suh, K. H.; Kang, S. G.; Jeong, S. K.; Kim, H. G. *Korean J. Chem. Eng.* **2004**, *21*, 806−810.

(46) Hu, T. L.; Chenfang, L.; Chiang, K. Y. *Adv. Environ. Res.* **2004**, *8*, 493−500.

(47) Mori, T.; Drennan, J.; Lee, J. H.; Li, J. G.; Ikegami, T. *Solid State Ionics* **2002**, *154*, 461−466.

(48) Mori, T.; Wang, Y. R.; Drennan, J.; Auchterlonie, G.; Li, J. G.; Ikegami, T. *Solid State Ionics* **2004**, *175*, 641−649.

(49) Kong, M.; Li, Y.; Chen, X.; Tian, T.; Fang, P.; Zheng, F.; Zhao, X. *J. Am. Chem. Soc.* **2011**, *133*, 16414−16417.

(50) Patsalas, P.; Logothetidis, S.; Sygellou, L.; Kennou, S. *Phys. Rev. B* **2003**, *68*, 1−13.

(51) Kim, S.; Lee, J. S.; Mitterbauer, C.; Ramasse, Q. M.; Sarahan, M. C.; Browning, N. D.; Park, H. J. *Chem. Mater.* **2009**, *21*, 1182−1186.